High-Resolution Elasticity Imaging for Tissue Engineering

N. Abraham Cohn, *Associate Member, IEEE*, B.-S. Kim, Ramon Q. Erkamp, *Student Member, IEEE*,
David J. Mooney, Stanislav Y. Emelianov, *Member, IEEE*, Andrei R. Skovoroda,
and Matthew O'Donnell, *Fellow, IEEE*

Abstract—An elasticity microscope provides high resolution images of tissue elasticity. With this instrument, it may be possible to monitor cell growth and tissue development in tissue engineering. To test this hypothesis, elasticity micrographs were obtained in two model systems commonly used for tissue engineering. In the first, strain images of a tissue-engineered smooth muscle sample clearly identified a several hundred micron thick cell layer from its supporting matrix. Because a one-dimensional mechanical model was appropriate for this system, strain images alone were sufficient to image the elastic properties. In contrast, a second system was investigated in which a simple one-dimensional mechanical model was inadequate. Uncultured collagen microspheres embedded in an otherwise homogeneous gel were imaged with the elasticity microscope. Strain images alone did not clearly depict the elastic properties of the hard spherical cell carriers. However, reconstructed elasticity images could differentiate the hard inclusion from the background gel. These results strongly suggest that the elasticity microscope may be a valuable tool for tissue engineering and other applications requiring the elastic properties of soft tissue at high spatial resolution (75 μm or less).

I. INTRODUCTION

IN A PREVIOUS set of publications, a system to image mechanical deformation fields at a fine scale (approximately 75 μm resolution for normal axial strain images) was described [1], [2]. We labeled this instrument an "elasticity microscope" because it can make images related to the elastic properties of tissue at a spatial resolution better than that resolvable by the human eye. It uses a modified ultrasonic scanner (50 MHz imaging) capable of tracking internal specimen motion due to an applied deformation. In this paper we explore the capabilities of this instrument for tissue engineering.

Tissues grown from cultured cells and synthetic matrices are being developed for a wide variety of applications,

such as skin for burn victims; replacement cartilage for the nose, ears, and joints; tendon and ligament replacement; and even cells to aid organ function, e.g., in the liver or kidney [3]. One method seeds then cultures cells on a collagen matrix or a polymer scaffolding. Tissue grows initially on the matrix or scaffold in vitro within a nutrient solution, then is implanted in the body or used as part of a replacement organ. The scaffold degrades slowly and produces a tissue construct that can function like the native organ.

Tissue engineers are greatly interested in noninvasively measuring the extent of cell growth and tissue development both to monitor samples and help improve culture methods. It would also be valuable to measure matrix development, such as elastin and hard tissues, which could determine the load-bearing capability of the implant. To improve growth techniques, measurements are required as a function of time. The current analysis method is cell histology. The specimen is sliced, stained, and put on a slide. However, this method kills cells. Different samples are prepared for histology and measured at varying times, but the high growth deviation between specimens makes analysis difficult. Ideally, tissue engineers need a system that can noninvasively monitor growth in the same specimen over time. The elasticity microscope and complementary instruments, such as ultrasonic and MRI microscopes, may provide this capability.

In this paper we explore this hypothesis with two examples from tissue engineering. The first uses a biodegradable polymer scaffolding made from polyglycolic acid (PGA) to engineer smooth muscle tissue [4]–[6]. Cells are grown in vitro for two weeks, then implanted on the back of a rat for another two weeks. At this point, the sample can be extracted for analysis. Typically, cell growth on the interior region of the scaffolding is limited by nutrient delivery. For smooth muscle, which has a high metabolic rate, one limiting nutrient is oxygen. The external region (100–300 μm) develops into new tissue with high cell density (approximately 10^8 cells/cm^3). In contrast, the inner section may be sparsely populated. After growth on an animal, the inner layer typically will form nonspecific scar tissue. Due to the expected elastic modulus difference between smooth muscle cells and scar tissue, and the nearly laminar geometry of the samples, the elasticity microscope may be able to visualize these layers directly from strain images. This possibility is examined in Section II.

N. A. Cohn, R. Q. Erkamp, S. Y. Emelianov, and M. O'Donnell are with the Biomedical Engineering and Electrical Engineering & Computer Science Departments, University of Michigan, Ann Arbor, MI 48109-2125 (e-mail: odonnel@umich.edu).

B.-S. Kim and D. J. Mooney are with the Chemical Engineering Department and Department of Dentistry, University of Michigan, Ann Arbor, MI 48109-2125.

A. R. Skovoroda is with the Institute of Mathematical Problems of Biology, Russian Academy of Sciences, Pushchino, Moscow Region, Russia 142292.

The second example uses a hard collagen sphere as the cell carrier. These structures, typically 200-300 μm in diameter, are often used in cell culture and gelatin preparations to test new growth techniques [7]. Unlike scaffolds, they do not conform to a laminar geometry. Consequently, strain images alone may not be sufficient to describe their mechanical properties; elastic modulus reconstruction may be needed to minimize geometry artifacts (i.e., strain variations related to the type of applied deformation and the geometry of inhomogeneities, not the mechanical properties of the beads and tissue layers directly). Both strain and reconstructed elasticity images for gelatin samples with embedded carrier beads are presented in Section III.

II. TISSUE ENGINEERED SAMPLES USING SCAFFOLDS

The specific samples investigated here may be adequately described by a layered model, in which soft tissue lamina grow on the surface of a hard matrix representing nonspecific scar tissue replacing the original scaffold. To test whether strain images obtained with the elasticity microscope described in [1], [2] can characterize such materials, layered phantoms with controlled mechanical properties were constructed and imaged.

A. Multiple Layer Phantoms

The stiffness of each section in a multiple-layer phantom was determined by gelatin concentration, in which layers were fabricated one at a time and added to the top of the phantom. Gels were started by dissolving 5 or 10% gelatin by weight in 60 ml of water for soft and stiff gel, respectively, then heated under constant stirring. Once dissolved, 10 ml (16% by volume) of ultra fine graphite particles acting as ultrasonic scatterers were added (mean particle size 9 μm; American Grease Stick Co., Muskegon, MI, model #MZ-25). The gel was cooled to just above the setting point while stirring constantly, then poured into a square 25 × 25 mm tank. A custom-fitted plug was inserted into the top of the mold. The plug left a specified gap to the bottom, which produced a gelatin layer with the desired thickness. Excess gelatin spilled out of the mold and was removed. This procedure was repeated multiple times, using plugs with different gaps, to create multiple-layered phantoms alternating in stiffness between soft and hard.

To quantify the elastic modulus (i.e., stiffness) of the phantom materials, the stiffness of three different gels—the soft and hard gels of the phantom, and a third even stiffer gel—was measured using the deformational system described in [8]. The gelatin concentrations in the three samples were 5%, 10%, and 15%, respectively. All samples also contained graphite, as described above. For each, the force/displacement curve was measured for five separate trials and averaged, and the elastic modulus was computed from the resulting averaged results using the methods described in [8]. Elastic modulus measurements are summarized in Table I.

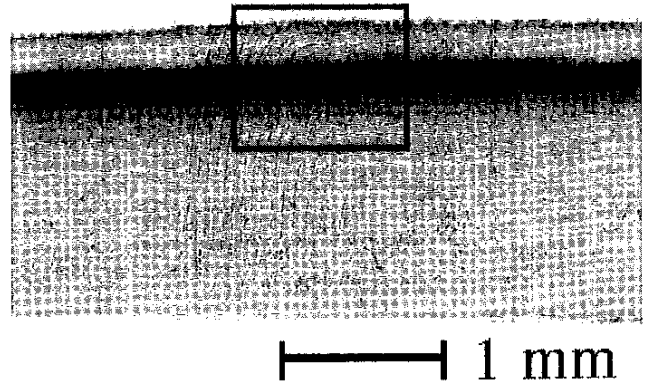| Specimen stiffness (% gelatin by weight)	Young's modulus (kPa)
Soft (5%)	3.9
Hard (10%)	13.7
Hardest (15%)	29.8

Fig. 1. Photo of three layer phantom constructed one layer at a time; the middle layer contains black graphite particles for visual contrast. The outlined box indicates the imaging region.

The measured elastic moduli for the gels used in this study fell within the range found in soft tissues [9]. Their specific stiffnesses were chosen for practical reasons. Softer gels were quite weak and ripped easily. Harder gels were more difficult to thoroughly mix with water, and their increased viscosity exacerbated bubble retention. No fixative, such as formaldehyde or glutaraldehyde, was used. Adding a fixative could provide significantly stiffer samples, but this would have complicated the analysis. Formaldehyde concentration was previously shown to affect the time-dependent stiffness of gelatin samples [10].

Typical images from our system are about 1 mm in both dimensions. Consequently, all layers were formed within the top millimeter of the sample. The phantoms were 2 mm deep, where the bottom gelatin layer was more than 1 mm thick and extended up into the imaging region. The three-layer phantom consisted of two hard layers with a soft layer in the middle. Its geometry is illustrated in Fig. 1, in which graphite was added only to the center layer for this photograph to provide visual contrast. In all ultrasonic and elasticity imaging experiments, every layer contained graphite as the scattering material. As depicted by the box

in Fig. 1, the scanning region contained two 400-μm thick hard outer layers sandwiching a 200-μm thick soft layer. The total thickness of the hard bottom region was 1.4 mm.

Fig. 2(a) displays the 50 MHz B-scan of the three-layer phantom over a 50 dB dynamic range. Note that the bottom layer, which extends more than 200 μm upward from the bottom of the image, is slightly darker than the layers above, presumably because the graphite concentration is reduced compared to the other layers. Also, note the bright echoes at layer interfaces. These reflections are caused by a combination of several factors: the surface of each layer forms a skin producing a slight acoustic impedance mismatch; in addition, some graphite particles settle during layer formation. The increased scatterer density across the bottom of that layer elevates the reflected signal. The interfaces are located 200 and 400 μm above the bottom of the image.

The normal axial strain is displayed in Fig. 2(b) over a range of 1 5%. For this image and all subsequent strain images, the gray scale is chosen such that white represents the largest strain value and black represents the smallest or most negative strain value. Because strain magnitude scaling depends on several factors, such as degree of preload, the optimal dynamic range for displaying each image will vary. The range of displayed strain values is chosen in each case to provide reasonable visible differentiation between regions. This may include a slight saturation of small portions of the image because of large variations in internal strain over the entire viewing area.

The bright band across Fig. 2(b) indicates a greater strain in the softer middle layer, as expected. Just above and below the high strain region, there are thin, dark areas representing low strain. They match well with the locations of a skin formed on the surfaces of the bottom two layers. Using the bright regions of the corresponding strain image as a guide, the layers in the B-scan can be more easily distinguished. This specimen provides a good example of a region difficult to identify solely with a B-scan that becomes readily apparent in a strain image. Fig. 2(c) shows a plot of the mean normal axial strain vs. depth, with bars illustrating $+/-$ one standard deviation in the measurement across the image. These variations include both physical variations in the specimen and measurement error.

B. Engineered Smooth Muscle Samples

Smooth muscle cells (SMCs) were isolated and cultured using a modification of the techniques described by Rothman et al. [11]. In brief, cells were isolated from aortas of 300–350 g adult male Lewis rats (Charles River Laboratories, Wilmington, MA) using an enzymatic dissociation. After fat, adventitia, and connective tissue surrounding the arteries were removed by blunt dissection, the SM tissue was cut into multiple small pieces and placed into a spinner flask containing an enzymatic dissociation buffer at 37°C. This buffer contained 0.125 mg/mL elastase (Sigma Chemical Co., St. Louis, MO), 1.0 mg/mL collagenase (CLS type I, 204 units/mg; Worthington Biochemical Corp., Free-
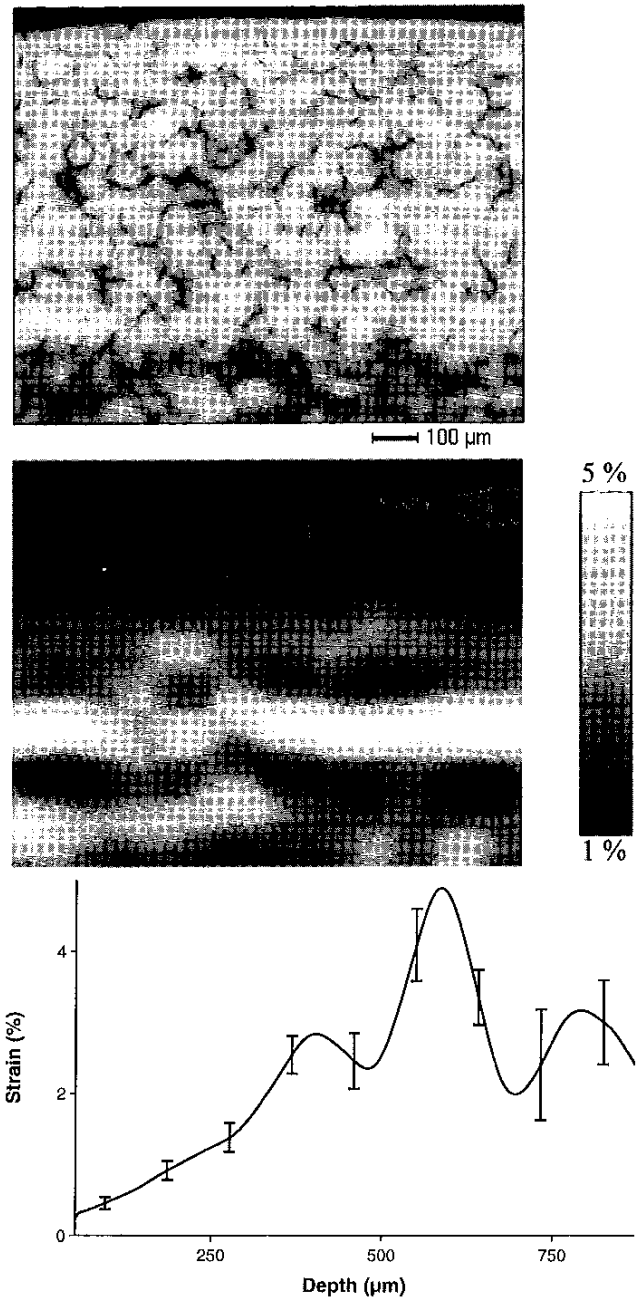
Fig. 2. Three layer phantom: (a) B-scan over a 50 dB dynamic range; (b) normal axial strain image, shown from 1% (black) to 5% (white); (c) plot of mean normal axial strain across the image, along with bars indicating $+/-$ one standard deviation.
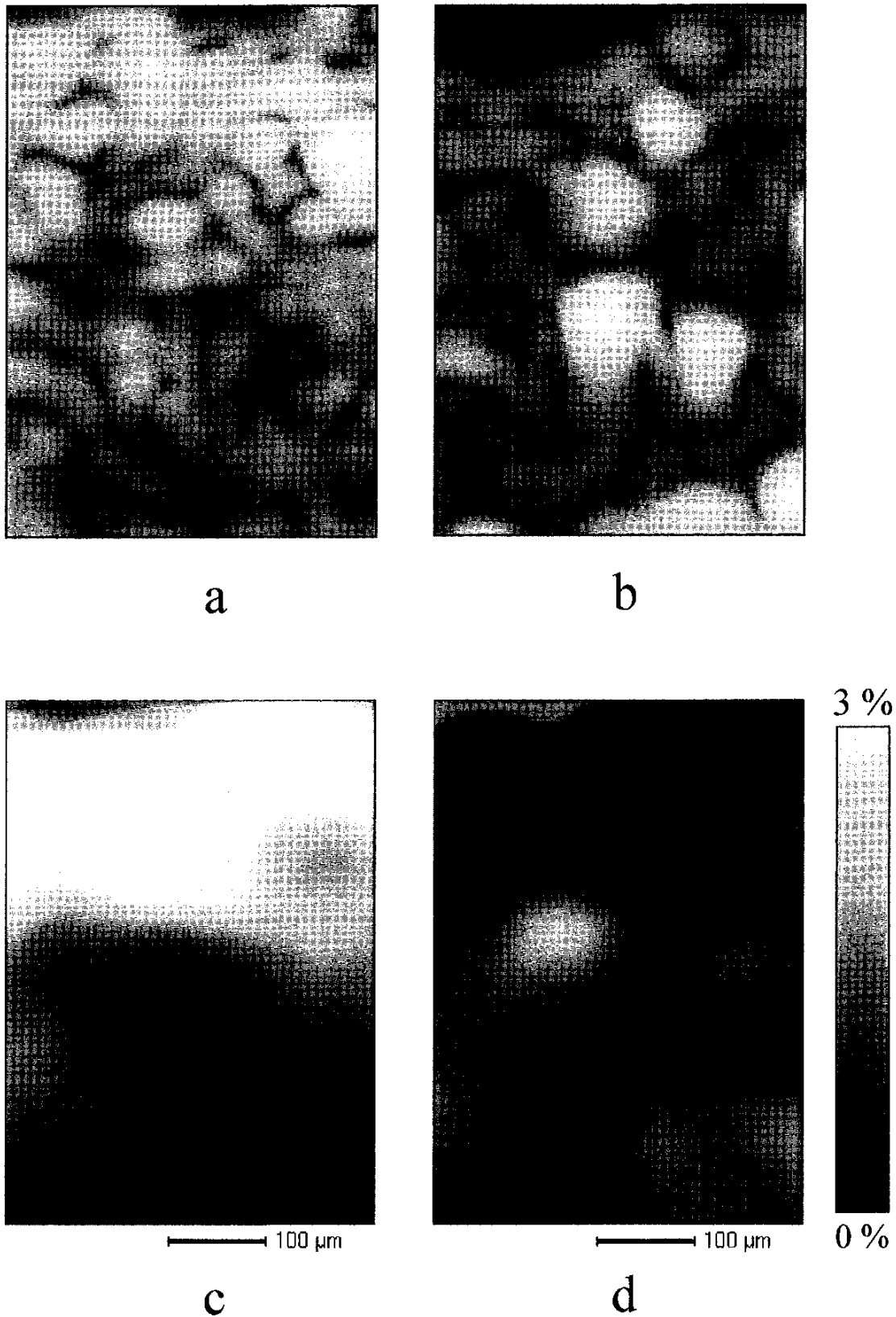
Fig. 3. Tissue-engineered smooth muscle specimens: B-scan displayed over a 50 dB dynamic range for (a) PGA scaffolding seeded and implanted with smooth muscle cells, and (b) PGA scaffolding implanted without seeding smooth muscle cells; normal axial strain image displayed from 0 to 3% for (c) seeded sample, and (d) unseeded sample.

hold, NJ), 0.250 mg/mL soybean trypsin inhibitor (type 1-S; Sigma Chemical Co.), and 2.0 mg/mL crystallized bovine serum albumin (Gibco/Life Technologies, Gaithersburg, MD). After 90 minutes of incubation, the suspension was filtered through a 100 μm Nitex filter (Tetko, Inc., Briarcliff Manor, NY) and centrifuged at 200 G for 5 minutes. The pellet was resuspended in Medium 199 (Sigma Chemical Co.) supplemented with 20% (v/v) fetal bovine serum (FBS; Gibco), 2 mM L-glutamine (Gibco), and 50 units/mL penicillin-streptomycin (Gibco). The cells were cultured on tissue culture plastic in a humidified 5% CO_2 atmosphere with the medium (Medium 199, 10% (v/v) fetal bovine serum, 50 units/mL penicillin-streptomycin) and changed every other day. Cells maintained through seven cycles were used for this study.

Polyglycolic acid (PGA) fibers (approximately 12 μm in diameter, Albany Int., Taunton, MA) were assembled into nonwoven arrays (3 mm thick) and used as matrices to engineer smooth muscle tissue. The bulk density of the PGA mesh was 50 mg/cc and the porosity was approximately 97%. Prior to cell seeding, matrices were cut into squares (25 × 25 mm) and prewet in Medium 199 containing 10% (v/v) FBS for 24 hours. For cell seeding, 1 mL of a cell suspension containing 2×10^7 cells/mL was injected into the polymer matrices in tissue culture dishes. After 4 and 10 hours, 2 mL and 20 mL of culture medium was added to each matrix, respectively. Seeded matrices were cultured in T-flasks (75 cm^2; Corning Inc., Corning, NY) in a humidified 5% CO_2 atmosphere, with the medium changed every other day for 2 weeks.

Polymer matrices, seeded or unseeded, were implanted into subcutaneous pockets in adult male Lewis rats for 2 weeks. Each sample was fixed in place by suturing the samples to the intramuscular layer with a nonabsorbable suture (Prolene 4-0; Ethicon, Inc., Somerville, NJ). Subsequently, samples were explanted for elasticity microscope experiments.

Based on the preparation procedures, the matrix geometry, and the pattern of cell growth, tissue-engineered scaffolds can be reasonably modeled as a layered medium, in which a middle layer represents the connective tissue (sparse cell region) and the upper and lower layers represent dense cell regions. The PGA scaffold was chosen to be 3.0-mm thick, a suitable dimension for the present elasticity microscope. After growing seeded cells, the outer cell layer is typically several hundred microns deep. Thus, a square 1-mm image should contain the outer cell layer and the inner sparse cell layer or scarred region.

Simple manual palpation of large samples confirmed that dense cell regions were softer than connective tissue. In particular, samples seeded with cells deformed more easily than unseeded samples. Unfortunately, the thin tissue engineered samples could not be evaluated with the same deformational system used to quantify the elastic modulus of the phantom materials; this problem is discussed more in Section IV. Nevertheless, a smooth muscle layer is expected to be softer than the scar tissue layer supporting it.

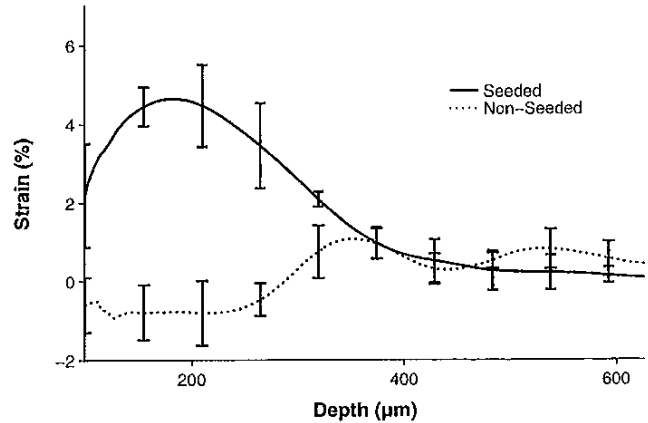To test the hypothesis that elasticity micrographs can

Fig. 4. Comparison of mean normal axial strain vs. depth for seeded and unseeded tissue-engineering samples, along with bars indicating +/- one standard deviation.

distinguish the top two layers, strain imaging experiments were performed on tissue-engineered smooth muscle and on scaffolding cultured and implanted in the same manner but without first seeding cells. The former experiment should illustrate the cell layering previously discussed; the latter experiment should serve as a control, exhibiting no smooth muscle or related cell growth. In addition, both specimens were examined histologically to compare with images from the elasticity microscope. For this analysis, samples were fixed in 10% (v/v) buffered formalin, paraffin embedded, sectioned, and stained with hematoxylin and eosin (H & E).

Fig. 3(a) (seeded smooth muscle specimen) and 3(b) (scaffolding sample cultured and implanted in the same manner but without first seeding cells) contrast 50 MHz B-scans of the tissue samples over a 50 dB dynamic range. There is a hint of a top layer in the seeded sample and some possible isolated scatterers in the unseeded sample. However, well defined, continuous structures are hard to identify in either B-scan. The normal axial strain image of the seeded specimen is shown in Fig. 3(c) over a 0–3% dynamic range. The strain is clearly higher in a layer at the top of the sample. Indeed, a softer layer about 200–300 μm thick was expected at the specimen surface. In contrast, the normal axial strain imaged over the same dynamic range is presented in Fig. 3(d) for the unseeded specimen. The strain is mostly smooth and small in magnitude, resulting in a nearly black image. In Fig. 4 the mean normal axial strain is plotted as a function of depth for both samples; the bars represent +/- one standard deviation across the image.

Fig. 5 shows histological sections from both tissue specimens (with and without seeded smooth muscle cells). A clear difference is seen between these two samples; histological analysis confirms an external layer in the cell-seeded implant with a high cell density and an inner lower density region [Fig. 5(a)]. Control matrices implanted without smooth muscle cells have a uniform appearance throughout, as expected, with no smooth muscle layer [Fig. 5(b)].
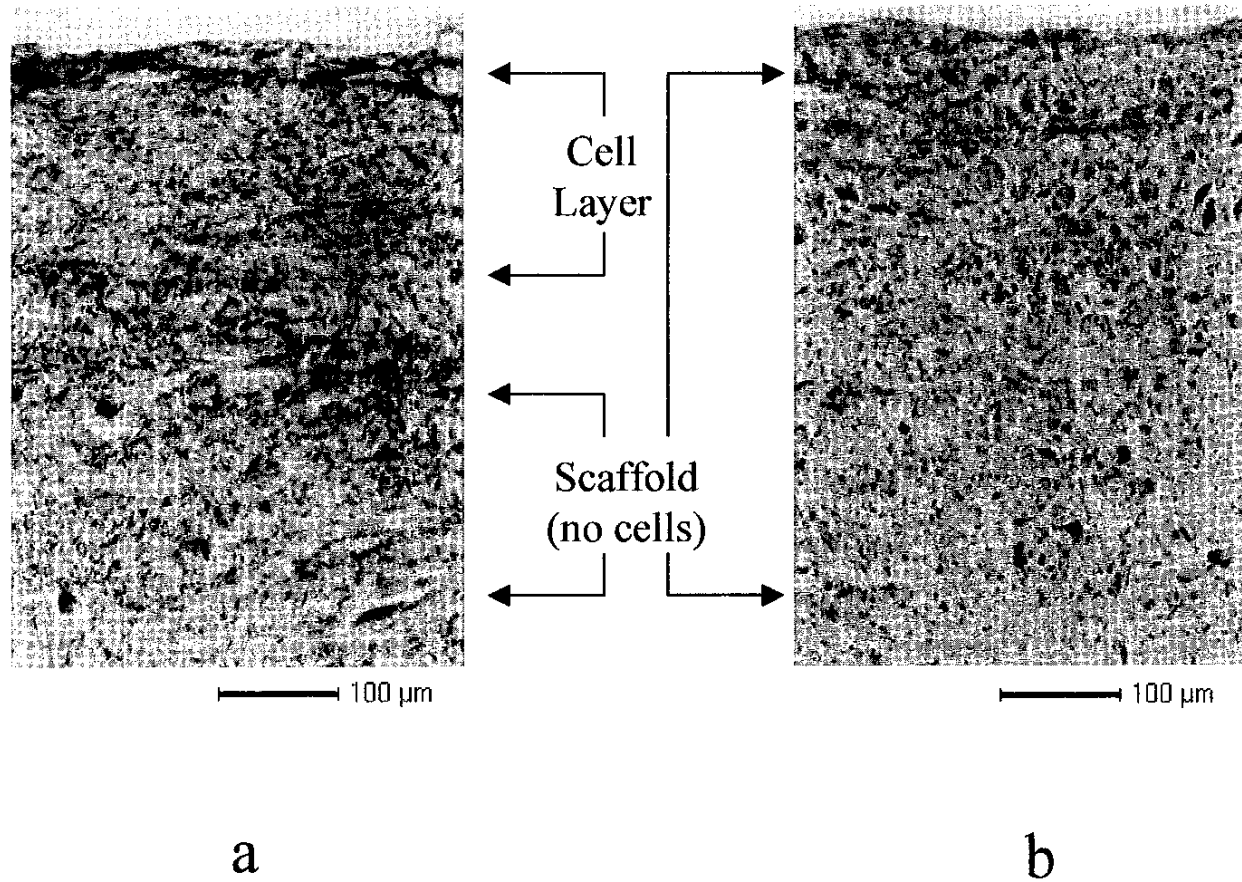
Fig. 5. Histology section stained with H & E: (a) polymer matrix seeded with smooth muscle cells, cultured, then implanted for 2 weeks. The cross section reveals a different structure between outer and inner layers; (b) polymer matrices without cell seeding and maintained in the same way; no significant layers are visible.

III. TISSUE ENGINEERED SAMPLES USING CARRIER BEADS

Spherical collagen beads are biocompatible cell carriers commonly used in tissue engineering for high density culture of adhesion-dependent cells [7]. Typical diameters are from 100–400 μm. Because the cell layers adhering to these beads are expected to be much softer than the hard bead itself, elasticity imaging may be able to monitor the thickness and mechanical properties of the cultured tissue.

A. Strain Images of Carrier Bead Samples

Uncultured carrier beads were added to an otherwise homogeneous gelatin phantom prepared for the elasticity microscope using the methods described in [1], [2]. The beads were made from CultiSpher-S, a highly cross-linked gelatin matrix, with diameters ranging from about 200–400 μm (HyClone Laboratories, Logan, UT). Because of their small size, the elastic modulus could not be evaluated with the deformation system described in [8]. However, manual palpation of the spheres indicated that they

were significantly harder than the background gel. A small volume of spheres (approximately 1 ml) was added to a soft gel mixture during the cooling phase. As verified by destructive testing following the experiment, a sufficient number of beads were dispersed throughout the phantom so that several beads always intersected the imaging plane.

Typical results for a gel sample of this type are presented in Fig. 6. The 50 MHz B-scan image is displayed over a 50 dB dynamic range in Fig. 6(a). The beads scatter ultrasound at this frequency, but produce speckle difficult to distinguish from the background. A normal axial strain image of the same phantom is shown in Fig. 6(b) over a 1–2.5% dynamic range. Low strain regions associated with the beads are easily identified. However, there are also high strain regions near the beads. They are part of the complete three-dimensional deformation pattern of the collagen inclusions and surrounding gel. As noted previously, a strain image is sufficient to characterize the elasticity distribution only if a one-dimensional model is valid [12]–[14]. A one-dimensional model is reasonable for the layered structures described in Section II, but it is inadequate to describe spherical bead inclusions.

Interpreting the strain image of an actual tissue-engineered sample with bead carriers may be very diffi-
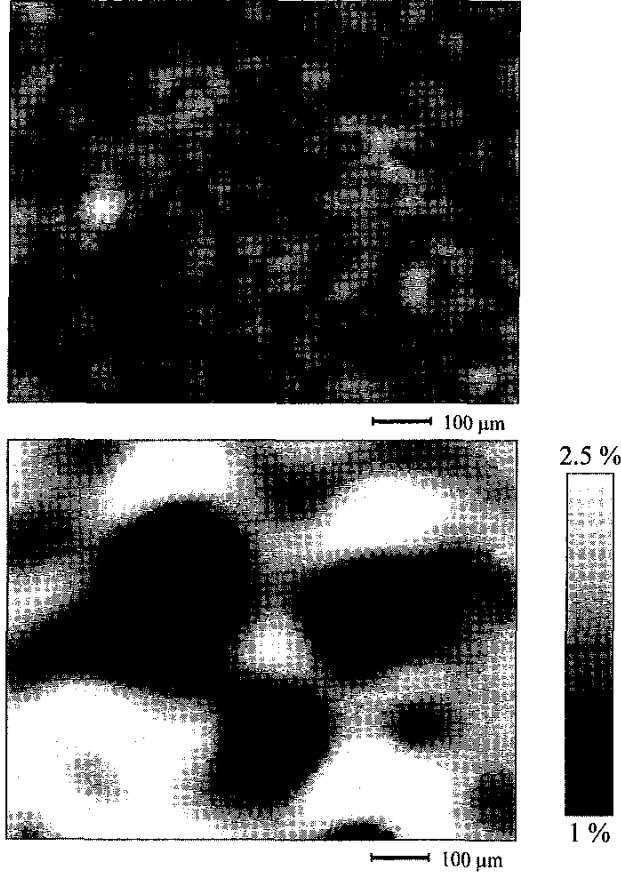
100 µm

2.5 %

1 %

100 µm

Fig. 6. Stiff collagen microspheres embedded in a softer homogeneous gelatin background: (a) B-scan over a 50 dB dynamic range; (b) normal axial strain image displayed over a dynamic range from 1% (black) to 2.5% (white).

cult based on the results presented in Fig. 6(b). For the uncultured beads used in this study, there is no soft tissue adhering to the surface. However, if this were a cultured sample, are the high strain regions surrounding the beads soft tissue, or are they simply irrelevant strain variations (i.e., "artifacts") compensating for the reduced strain within the beads? To help answer this question, we have explored elasticity reconstruction (i.e., reconstruction of the elastic modulus) based on a two-dimensional mechanical model. A two-dimensional model cannot fully describe deformations of a sphere; but, as demonstrated in the next section, it can be used to formulate a reconstruction algorithm greatly reducing artifacts in strain images.

B. Elasticity Reconstruction

The deformation system for the elasticity microscope provides a nearly uniform axial load (i.e., primary deformation along the ultrasonic beam direction). Consequently, it produces a plane strain state in the ultrasound image plane for structures with uniform elastic modulus perpendicular to this plane. In a plane strain state, the out of plane displacement component is spatially uniform

(i.e., uniform motion into and out of the image plane), and all three displacement components do not vary significantly as functions of the out-of-plane coordinate. For more general three-dimensional objects, the deformation approximates a plane strain state. Later, we discuss the applicability of this model to the true three-dimensional problem presented by the beads.

As shown in [14], [15], reconstructing the elasticity distribution for a plane strain state in an incompressible material such as soft tissue reduces to solving the following second order hyperbolic partial differential equation:

$$(\mu \varepsilon_{xy})_{,xx} - (\mu \varepsilon_{xy})_{,yy} + 2(\mu \varepsilon_{yy})_{,xy} = 0. \qquad (1)$$

The function $\mu(x, y)$ is the unknown spatial distribution of the shear elastic modulus (i.e., elasticity), and strain components ε_{yy} and ε_{xy} are related to the displacement components as:

$$\varepsilon_{yy} = v_{,y},$$
$$\varepsilon_{xy} = (u_{,y} + v_{,x})/2. \qquad (2)$$

Here $\mathbf{U} = \mathbf{U}(x, y, z) = (u, v, w)$ is the displacement vector in Cartesian coordinates x, y, z, where the ultrasound propagation direction is along the y axis and imaging is performed in the x-y plane. The lower index after a comma means differentiation with respect to the corresponding spatial coordinates.

The equilibrium equation expressed in (1) also can be presented in integral form:

$$\delta(x, y) \equiv 2 \big[\varepsilon_{yy}\mu - (\varepsilon_{yy}\mu)|_{x_0}$$
$$- (\varepsilon_{yy}\mu)|_{y_0} + (\varepsilon_{yy}\mu)|_{x_0, y_0} \big] +$$
$$\int_{y_0}^{y} \big[(\varepsilon_{xy}\mu)_{,x} - \{(\varepsilon_{xy}\mu)_{,x}\}|_{x_0} \big] dy$$
$$- \int_{x_0}^{x} \big[(\varepsilon_{xy}\mu)_{,y} - \{(\varepsilon_{xy}\mu)_{,y}\}|_{y_0} \big] dx = 0, \qquad (3)$$

where the notations $f|_{x_0} = f(x_0, y)$ and $f|_{y_0} = f(x, y_0)$ have been employed. (3) is stated in terms of a functional $\delta(x, y)$, where the goal of the reconstruction algorithm is to find the shear modulus distribution $\mu(x, y)$ forcing $\delta(x, y)$ to approach zero in some average sense based on noisy deformation data [16].

To evaluate all terms in (3), the in-plane displacement vector is needed throughout the image. Both components were estimated using the two-dimensional speckle tracking procedure described in [1], [2]. Due to the reduced quality of lateral displacement estimates, however, these data were further processed with the incompressibility methods described in [17], [18] prior to elasticity reconstruction. Incompressibility processing also assumed a plane strain state.

For any region of interest (ROI) within the object, the elasticity distribution $\mu(x, y)$ is first specified along the boundary of the ROI. If the elastic modulus is constant

along two characteristic curves (i.e., two intersecting lines within the ROI for this geometry), the reconstructed image is the elastic modulus relative to the actual boundary modulus μ_0. The constant μ_0 along these curves is the elastic modulus of the gel. Thus, the reconstructed image is the elastic modulus relative to that of the gel. In general, curves of nearly constant elastic modulus far from the objects of interest can be identified from the strain image using the boundary detection methods described in [14].

The elasticity distribution is reconstructed by minimizing the error functional $\delta(x, y)$ across the ROI given the boundary distribution and the measured displacements and computed strains. The specific minimization procedure is described in [16]. Given an image of the two-dimensional displacement field, the elastic modulus image was reconstructed in about 100 seconds on a low-end, engineering workstation (Sparc 10; Sun Microsystems, Palo Alto, CA).

Deformation data from two previous phantom measurements were used to test the proposed reconstruction algorithm. One phantom was a homogeneous gel. The second was a nearly homogeneous gel with a single, cylindrical hard inclusion made from rubber (Super Soft Plastic, stock # 8228SS; MF Manufacturing Corp., Fort Worth, TX), in which the cylinder axis was perpendicular to the image plane. The inclusion diameter was 265 μm, and its elastic modulus was estimated to be 16 times greater than that of the gel [2]. Deformations of these phantoms closely approximated a plane strain state. Fabrication methods, B-scan, and strain images are presented in [1], [2].

Reconstructed images of the relative elasticity (i.e., elastic modulus relative to that of the gel) are presented in Fig. 7 for the two test phantoms. The homogeneous phantom is presented in Fig. 7(a) over a logarithmic gray scale spanning a relative modulus from 1/6 to 6. The phantom with a single hard inclusion is presented in Fig. 7(b) over the same display dynamic range. The size, shape, and extent of the inclusion are clearly seen in this figure. In addition, the average value of the relative modulus within a small region centered on the inclusion is about 13, close to the expected value of 16.

The same reconstruction algorithm was then applied to deformation data from the bead sample. The reconstructed image of the relative elasticity is presented in Fig. 8, in which a logarithmic gray scale spanning a relative modulus from 1/3 to 3 is used. Three hard beads can be identified. As expected, the average value of the reconstructed modulus differs in the three beads because different cross sections intersect the imaging plane (i.e., a two-dimensional model cannot completely describe the true three-dimensional deformation pattern associated with each bead). Unlike the strain image of Fig. 6(b), however, the reconstructed relative modulus image clearly shows only the hard beads within a nearly uniform background.
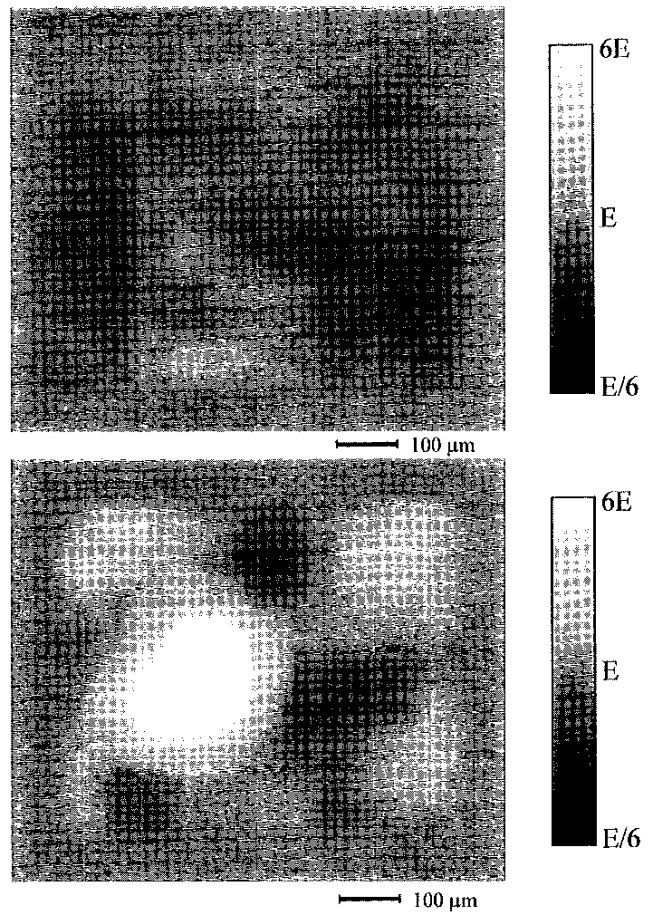

Fig. 7. Reconstructed relative elasticity images of two test phantoms: (top) homogeneous gel; (bottom) otherwise homogeneous gel with a hard, cylindrical (i.e., circular cross section) inclusion. Both images are displayed on a logarithmic gray scale spanning a relative modulus from 1/6 to 6.0.
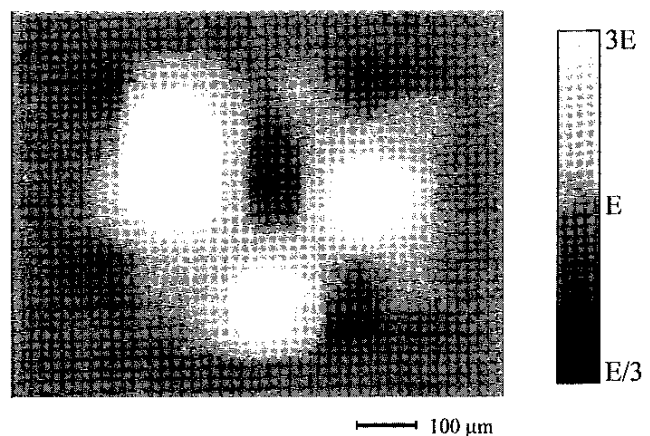

Fig. 8. Reconstructed relative elasticity image of the collagen bead sample presented in Fig. 6 over a logarithmic gray scale spanning a relative modulus from 1/3 to 3.

IV. DISCUSSION

Experiments on a three-layer phantom showed that strain alone was sufficient to characterize the elastic properties of layered, planar structures imaged with the elasticity microscope. The plot of mean normal axial strain [Fig. 2(c)] demonstrates a shift to higher strain within the soft layer that clearly exceeds the standard deviation in the image. Interestingly, the inhomogeneous strain profile is similar to the homogenous one but slightly lower at all depths, except for the position of the soft layer; it then increases significantly. This behavior agrees with our expectations; because, for a given total deformation, increased strain in one region should be balanced by decreased strain elsewhere. This also can be seen in the strain image of the bead sample [Fig. 6(b)] in which high strain regions compensate for the decreased strain in the beads.

In analogy to the multiple-layer phantom, Fig. 3(c) shows that a thin cell layer can be differentiated from its supporting matrix based solely on a high resolution strain image. From this image, we predict a softer layer on the surface of the tissue engineered smooth muscle. As supported by the histology section [Fig. 5(a)], the top layer consists of developed smooth muscle and tissue matrix, contrasted with the stiffer connective tissue and scarring below. The specimen without implanted smooth muscle cells provides both a more uniform strain profile [Fig. 3(d)] and more uniform histology consisting primarily of connective tissue [Fig. 5(b)]. The difference in normal axial strain between the two samples is further illustrated in Fig. 4; the seeded sample has a high strain in the surface layer far exceeding the standard deviation of strain measurements. In both cases, the biodegradable PGA scaffolding was partially degraded after the 4 week growth period prior to the experiment, and most likely it no longer provided any significant stiffness to the samples. Remnants of scaffold are visible in the histology sections. These results demonstrate that strain images alone can identify layers of cell growth and tissue development in laminar samples if adjacent layers have different stiffness.

In contrast, high resolution strain images of the collagen microsphere sample cannot clearly identify the hard beads because of strain artifacts [Fig. 6(b)]. Elasticity reconstruction algorithms developed for a plane strain state have been applied to two-dimensional displacement data to image the elastic modulus distribution in this sample (Fig. 8). Even with this simplistic model, the reconstructed elasticity image clearly shows the bead extent and a nearly uniform background. The magnitude of the reconstructed elastic modulus inside each sphere, however, is not the same because the cross section of each sphere intersecting the image plane is different.

To estimate the magnitude of the reconstruction error due to a two-dimensional approximation of a three-dimensional inclusion, the three-dimensional deformation pattern for a spherical inclusion in an otherwise homogeneous medium under the current loading condition was analyzed. As discussed in [13], Goodier's classic solution

[19] can predict the true deformation pattern in any plane intersecting the inclusion. Given this pattern, the elastic modulus can be reconstructed under a plane strain approximation based on stress continuity conditions on the boundary of the spherical inclusion and compared to the actual modulus distribution [14]. Such an analysis predicts that the reconstructed relative modulus $\mu_{2\text{-}D}$ within the sphere is related to the actual relative modulus μ as:

$$\mu_{2\text{-}D} = \mu - (\mu - 1)\xi^2, \qquad (4)$$

where ξ is the distance (relative to the sphere radius, and, therefore, ranging from 0 to 1) between the image plane and the central spherical cross section. If the image plane intersects the great circle of the sphere (i.e., $\xi = 0$), the reconstructed modulus equals the actual modulus. Otherwise, the reconstructed modulus underestimates the true modulus, in which the underestimation is greater the farther the imaging plane is from the central plane of the sphere. This relationship is apparent in Fig. 8; the reconstructed modulus is clearly smaller in the beads with smaller cross sections.

Although the elastic modulus within the spherical inclusions was not always accurately reconstructed assuming a plane strain state, strain artifacts were greatly reduced with reconstruction. In general, two-dimensional elasticity reconstruction can reduce artifacts associated with a one-dimensional interpretation of a strain image. The reconstructed elastic modulus distribution, however, is not artifact free if the plane strain approximation is grossly violated. Consequently, reconstructed modulus images cannot fully replace strain images until full three-dimensional deformation patterns are imaged. Nevertheless, reconstruction is an important step in elasticity imaging. When carefully applied, a reconstructed modulus image augments a strain image to better characterize the elasticity distribution within soft tissue.

The elastic properties of the tissue-engineered samples used here could be qualitatively assessed through palpation; but the elastic modulus could not be quantified with the current force-deformation system (described in [8]). This system measured the elastic properties of the phantom materials but could not handle the tissue-engineered samples because they were too small. Future work will attempt to dramatically reduce the minimum sample volume (currently about 0.5 cm^3) for this system.

A 50 MHz ultrasound imaging system was used for the results reported here. Because the speckle tracking and elasticity reconstruction methods developed first at lower frequencies (5 MHz) scaled well to this higher frequency, it may be possible to apply similar methods at frequencies of 500 MHz and up. Obviously, there will be significant technical problems in scaling from 50 to 500 MHz, as there were in scaling from 5 to 50 MHz. Elasticity reconstruction methods also must be reformulated for these reduced spatial dimensions. Nevertheless, imaging the elastic properties of tissue at cellular dimensions is an exciting prospect that should accelerate technical developments.

V. SUMMARY

The elasticity microscope can produce high resolution images of soft tissue elasticity. We have used this instrument to investigate two key problems in tissue engineering. For one case in which a one-dimensional mechanical model was appropriate, strain images were able to directly identify smooth muscle cell layers cultured on a hard, scar tissue matrix. For a second case in which a one-dimensional mechanical model was inadequate, elasticity reconstruction of deformation data were required to clearly identify hard collagen microspheres in a uniform gel. In addition to the specific examples presented here, many possible applications could benefit from the present instrument, or similar systems designed with a higher frequency transducer. Specifically, we are actively investigating several potential areas, including measurement of cell and matrix development in tissue engineering and analysis of the upper skin layers for dermatology. In addition, we are examining the neural transduction mechanism in the finger by relating in vivo mechanical strain images to mechanoreceptive nerve ending response [20].

ACKNOWLEDGEMENTS

REFERENCES

[1] N. A. Cohn, S. Y. Emelianov, M. A. Lubinski, and M. O'Donnell, "An elasticity microscope. Part I: Methods," IEEE Trans. Ultrason., Ferroelect., Freq. Contr., vol. 44, no. 6, pp. 1304–1319, 1997.

[2] N. A. Cohn, S. Y. Emelianov, and M. O'Donnell, "An elasticity microscope. Part II: Experimental results," IEEE Trans. Ultrason., Ferroelect., Freq. Contr., vol. 44, no. 6, pp. 1320–1331, 1997.

[3] R. Langer and J. P. Vacanti, "Tissue engineering," Science, vol. 260, pp. 920–926, 1993.

[4] D. J. Mooney, C. L. Mazzoni, C. Breuer, K. McNamara, D. Hern, J. P. Vacanti, and R. Langer, "Stabilized polyglycolic acid fibre-based tubes for tissue engineering," Biomaterials, vol. 17, no. 2, pp. 115–124, 1996.

[5] A. J. Putnam and D. J. Mooney, "Tissue engineering using synthetic extracellular matrices," Nature Med., vol. 2, no. 7, pp. 824–826, 1996.

[6] B.-S. Kim, A. J. Putnam, T. J. Kulik, and D. J. Mooney, "Optimizing seeding and culture methods to engineer smooth muscle tissue on biodegradable polymer matrices," Biotechnol. Bioeng., vol. 57, pp. 46–54, 1998.

[7] M. Butler, "A comparative review of microcarriers available for the growth of anchorage-dependent animal cells," in Animal Cell Biotechnology. vol. 3, R. E. Spier and J. B. Griffith, Eds. London: Academic, 1988, pp. 285–305.

[8] R. Q. Erkamp, P. Wiggins, A. R. Skovoroda, S. Y. Emelianov, and M. O'Donnell, "Measuring the elastic modulus of small tissue samples," Ultrason. Imag., vol. 20, pp. 17–28, 1998.

[9] A. P. Sarvazyan, A. R. Skovoroda, S. Y. Emelianov, J. B. Fowlkes, J. G. Pipe, R. S. Adler, R. B. Buxton, and P. L. Carson, "Biophysical bases of elasticity imaging," Acoust. Imaging, vol. 21, pp. 223–240, 1995.

[10] T. J. Hall, M. Bilgen, M. F. Insana, and P. Chaturvedi, "Phantoms for elastography," in Proc. IEEE Ultrason. Symp., 1996, pp. 1193–1196.

[11] A. Rothman, T. J. Kulik, M. B. Taubman, B. C. Berk, C. W. J. Smith, and B. Nadal-Ginard, "Development and characterization of a cloned rat pulmonary arterial smooth muscle cell line that maintains differentiated properties through multiple subcultures," Circulation, vol. 86, pp. 1977–1986, 1992.

[12] J. Ophir, I. Cespedes, H. Ponnekanti, Y. Yazdi, and X. Li, "Elastography: A quantitative method for imaging the elasticity of biological tissues," Ultrason. Imag., vol. 13, pp. 111–134, 1991.

[13] A. R. Skovoroda, S. Y. Emelianov, M. A. Lubinski, A. P. Sarvazyan, and M. O'Donnell, "Theoretical analysis and verification of ultrasound displacement and strain imaging," IEEE Trans. Ultrason., Ferroelect., Freq. Contr., vol. 41, no. 3, pp. 302–313, 1994.

[14] A. R. Skovoroda, S. Y. Emelianov, and M. O'Donnell, "Tissue elasticity reconstruction based on ultrasonic displacement and strain images," IEEE Trans. Ultrason., Ferroelect., Freq. Contr., vol. 42, no. 4, pp. 747–765, 1995.

[15] S. Y. Emelianov, A. R. Skovoroda, M. A. Lubinski, and M. O'Donnell, "Reconstructive elasticity imaging," Acoust. Imaging, vol. 21, pp. 241–252, 1995.

[16] A. R. Skovoroda, M. A. Lubinski, S. Y. Emelianov, and M. O'Donnell, "Reconstructive elasticity imaging for large deformations," IEEE Trans. Ultrason., Ferroelect., Freq. Contr., vol. 46, no. 3, pp. 523–535, 1999.

[17] M. A. Lubinski, S. Y. Emelianov, K. R. Raghavan, A. E. Yagle, A. R. Skovoroda, and M. O'Donnell, "Lateral displacement estimation using tissue incompressibility," IEEE Trans. Ultrason., Ferroelect., Freq. Contr., vol. 43, pp. 247–256, 1996.

[18] A. R. Skovoroda, M. A. Lubinski, S. Y. Emelianov, and M. O'Donnell, "Nonlinear estimation of the lateral displacement using tissue incompressibility," IEEE Trans. Ultrason., Ferroelect., Freq. Contr., vol. 45, pp. 491–503, 1998.

[19] J. N. Goodier, "Concentration of stress around spherical and cylindrical inclusions and flaws," Trans. ASME, vol. 55, pp. 39–44, 1933.

[20] M. A. Srinivasan and K. Dandekar, "An investigation of the mechanics of tactile sense using two-dimensional models of the primate fingertip," Trans. ASME, vol. 118, pp. 48–55, 1996.
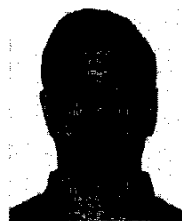
Nabi Abraham Cohn (S'95–AM'92) was born in 1970. He received the dual B.S.E. degree in Biomedical and Electrical Engineering from Duke University in 1992, where he was an NSF/ERC undergraduate research fellow. At the University of Michigan, Ann Arbor, he received M.S. degrees in Bioengineering and Electrical Engineering in 1994 and 1996, respectively, followed by a Ph.D. in Biomedical Engineering in 1997. He held a graduate fellowship from the Whitaker Foundation.

His research at the University of Michigan Biomedical Ultrasonics Laboratory utilized 50-MHz ultrasound to obtain high resolution elasticity imaging. This included design and development of mechanical, electrical, and algorithmic components of the experimental system.

Since 1997, Dr. Cohn has been developing image quality improvements for computed tomography systems at Marconi Medical Systems, Cleveland. He is currently a technical engineering manager in charge of image calibration, image reconstruction, and prototype simulation.

Ramon Q. Erkamp (S'96) was born in Den Helder, The Netherlands. He received the Ing. degree in Electrical Engineering (specializing in digital systems) in 1992 from the Hogeschool Enschede, The Netherlands. In 1995, he received the M.S. degree in Biomedical Engineering (bioelectrical major), and, in 1997, he received the M.S. degree in Electrical Engineering (signal processing major), both from the University of Michigan, Ann Arbor. Currently, he is pursuing a Ph.D. in Biomedical Engineering at the Biomedical Ultrasonics Laboratory, University of Michigan, Ann Arbor. His interests include medical imaging, (nonlinear) ultrasound elasticity imaging, signal processing, direct mechanical elasticity measuring, instrumentation design, and VLSI algorithm implementations.

Stanislav Y. Emelianov (M'94) was born in May 1966. He received the B.S. and M.S. degrees in physics in 1986 and 1989, respectively, from Moscow State University, and the Institute of Mathematical Problems of Biology of the Russian Academy of Sciences, Russia.

In 1989, he joined the Institute of Mathematical Problems of Biology, where he was engaged in both mathematical modeling of soft tissue biomechanics and experimental studies of noninvasive methods in medical diagnostics based on tissue elasticity variations. Following his graduate work, he moved to the University of Michigan, Ann Arbor, as a post-doctoral fellow in the Electrical Engineering and Computer Science Department working on applications of imaging systems for medical diagnosis and nondestructive testing. Dr. Emelianov is currently a research scientist in the Biomedical Ultrasonics Laboratory at the University of Michigan and involved primarily in the theoretical and practical aspects of ultrasound elasticity imaging. He is the author of several scientific papers. His research interests are in the areas of tissue biomechanics, medical imaging systems, and nondestructive material testing.
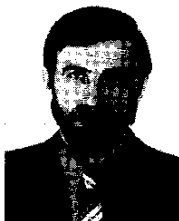
Andrei R. Skovoroda received the B.S. and M.S. degrees in mathematics and mechanics in 1973 and 1975, respectively, from the Novosibirsk State University, USSR, and the Ph.D. degree in 1985 from the Moscow State University, USSR.

From 1975 to 1977 he was a lecturer in theoretical mechanics at the College of Textile Technology, Barnaul, USSR. From 1977 to 1980 he was a Ph.D. researcher at the subfaculty of Plasticity of the Moscow State University, where he worked on the dynamic behavior of plates under blast-type loading. In 1981 he held an appointment as a junior research associate at the Laboratory of Mathematical Modeling of the Research Computing Center of the USSR Academy of Sciences (the present name: Institute of Mathematical Problems of Biology, Russian Academy of Sciences), where he developed efficient mathematical methods to solve the differential equations of the theory of elasticity. In 1986 he became a senior research associate and was scientific secretary at the same institute from 1988 to 1993. He is currently head of the Laboratory of Mathematical Problems in Biomechanics and works on the biomechanics of soft tissue.

Dr. Skovoroda has authored and co-authored more than 90 articles for archival publications and papers presented at all-union and international meetings.

Matthew O'Donnell (M'79 SM'84 F'93) has a B.S. and Ph.D. in Physics from the University of Notre Dame (1972 and 1976, respectively). Following his graduate work, Dr. O'Donnell moved to Washington University in St. Louis as a postdoctoral fellow in the Physics Department, working on applications of ultrasonics to medicine and non-destructive testing. He subsequently held a joint appointment as a Senior Research Associate in the Physics Department and a Research Instructor of Medicine in the Department of Medicine at Washington University. In 1980, he moved to General Electric Corporate Research and Development Center in Schenectady, New York, where he continued to work on medical electronics, including MRI and ultrasound imaging systems. During the 1984 and 1985 academic year, he was a visiting fellow in the Department of Electrical Engineering at Yale University, investigating automated image analysis systems. In a bold move during 1990, Dr. O'Donnell became Professor of Electrical Engineering & Computer Science at the University of Michigan in Ann Arbor, Michigan. Since 1997, he's held a joint appointment as Professor of Biomedical Engineering at Michigan, and, in 1998, he was named the Jerry W. and Carol L. Levin Professor of Engineering. Currently, he is the Chair of the Biomedical Engineering Department. His most recent work has explored new imaging modalities in biomedicine, including elasticity imaging, in vivo microscopy, and catheter-based devices.

Dr. O'Donnell is a member of Sigma Xi, the American Physical Society, and is a fellow of both the IEEE and the AIMBE. He has authored or coauthored over 140 archival publications, including two that received best paper awards. He has had numerous presentations at national meetings and holds 40 patents.